

DOI: 10.1002/((please add manuscript number))

Article type: Communication

Electron mobility of 24cm²/Vs in PbSe colloidal quantum dot superlattices

*Daniel M. Balazs, Bartosz M. Matysiak, Jamo Momand, Artem G. Shulga, Maria Ibáñez, Maksym V. Kovalenko, Bart J. Kooi, Maria Antonietta Loi**

Dr. D. M. Balazs, B. M. Matysiak, Dr. J. Momand, A. G. Shulga, Prof. B. J. Kooi, Prof. M. A. Loi*

Zernike Institute for Advanced Materials, University of Groningen, Nijenborgh 4, 9747AG, Groningen, Netherlands

E-mail: m.a.loi@rug.nl

Dr. M. Ibáñez, Prof. M. V. Kovalenko

Department of Chemistry and Applied Biosciences, ETH Zürich, Vladimir Prelog Weg 1, Zürich 8093, Switzerland

and

Empa-Swiss Federal Laboratories for Materials Science and Technology, Überlandstrasse 129, Dübendorf 8600, Switzerland

Keywords: colloidal quantum dots, superlattice, self-assembly, transport, electrolyte-gated transistor

Colloidal quantum dots are nanoscale building blocks for bottom-up fabrication of semiconducting solids with tailorable properties beyond the possibilities of bulk materials. Achieving ordered, macroscopic crystal-like assemblies has been in the focus of researchers for years, since it would allow for exploitation of the quantum confinement-based electronic properties with tunable dimensionality. Lead-chalcogenide colloidal quantum dots show especially strong tendencies to self-organize into 2D superlattices with micron-scale order, making the array fabrication fairly simple. However, most works concentrate on the fundamentals of the assembly process, and none have investigated the electronic properties and their dependence on the nanoscale structure induced by different ligands. In this paper, we discuss how different chemical treatments on the initial superlattices affect the nanostructure, the optical and the electronic transport properties. Transistors with average two-terminal electron mobilities of 13 cm²/Vs and contactless mobility of 24 cm²/Vs are obtained for small area superlattice FETs. Such mobility values are the highest reported for

CQD devices wherein the quantum confinement is substantially present, and are comparable to those reported for heavy sintering. The considerable mobility with the simultaneous preservation of the optical band gap displays the vast potential of colloidal QD superlattices for optoelectronic applications.

Introduction

Colloidal quantum dots (CQDs) are semiconductor nanocrystals in the quantum confinement regime, where the particle size is significantly smaller than the exciton Bohr-radius in the material. The interest towards this class of materials stems from their prospects in photovoltaic and optoelectronic applications. Solution-processed solar cells with over 11% power conversion efficiencies have been fabricated based on PbS CQDs exploiting their high absorbance and the size-tunability of the band gap,^[1] field-effect transistors (FETs) based on colloidal nanocrystals were shown to exhibit excellent performance,^[2] PbS CQD solids can be used to fabricate highly efficient ambipolar inverters,^[3] and light-emitting field-effect transistors (LEFETs) show the potential in light-coupled electronics applications.^[4]

In all reported applications, the arrays of Pb- or Cd-chalcogenide CQDs are dense, but rather disordered, or exhibit only short-range order.^[5, 6] The energetic disorder (stemming from size polydispersity, positional disorder and varying coupling strength) give rise to properties closer to those of amorphous solids, like conjugated polymers, rather than of bulk crystals.^[7] The chances of exploiting the unique properties of these materials would be much greater if one achieved coherent transport throughout an ordered array of quantum dots.^[8]

Highly ordered CQD superlattices can be formed by drying a solution on a liquid surface.^[9-12] Orientation of lead-chalcogenide CQDs in a superlattice can be controlled by adjusting the reactivity of the subphase through the choice of solvent, by adding chemical species or by changing the temperature.^[11, 13-15] This possibility stems from the faceted nature of the CQDs;

crystal orientation-specific interactions and different binding energy of the ligands at the main crystallographic facets drive the orientation process.^[16-22] While much work has been done on the formation mechanism and properties of the superlattices on solid substrates,^[17, 18, 20, 21, 23-29] fewer studies investigated liquid interface-grown layers,^[7, 11, 15, 22, 30-33] and even fewer have been devoted to study the structure-property relation in these samples.^[7, 30, 31, 33] Whitham *et al.* measured the effect of disorder on charge localization in PbSe CQD superlattices, they deduced a carrier localization over 2-3 quantum dots in their system and calculated a disorder limit below which band-like, coherent transport is expected to occur.^[7] Evers *et al.* observed a similar degree of delocalization in samples prepared using a slightly different method.^[15] Alimoradi Jazi *et al.* observed contactless mobilities averaging to $3.6 \text{ cm}^2/\text{Vs}$ ^[33], setting the superlattices on par with the best spin-coated PbSe samples.^[18, 29, 34, 35] However, the transport properties have so far not reached the quality expected from ordered, strongly coupled arrays, and no complete work has been done on connecting the electronic coupling, the nanostructure and the electrical transport properties in superlattices, especially not in samples formed using different ligands.

In this work, we aimed to fill this gap with a systematic analysis on the charge transport in PbSe CQD superlattices and its dependence on the nanoscale structure of the samples. We fabricate samples using four different ligands that result in slightly different nanoscale organization of the CQDs, and characterize the electron transport properties of the superlattices in ionic gel-gated field-effect transistors (FETs). A large improvement in the electron mobility up to $24 \text{ cm}^2/\text{Vs}$ is observed upon increasing the width of the interparticle bridges, “necks”. The samples with higher number, but narrower necks show mobilities an order of magnitude lower, suggesting that the neck width is the dominant factor over the number and homogeneity of the connections for efficient charge transport. This is the first evidence of such high mobilities achieved in ordered networks of CQDs and opens the way to further exploitation of these solids in (opto)electronics.

Results and discussion

We fabricated mono- and multilayer PbSe CQD superlattices (SLs) by assembling the particles on top of ethylene glycol (EG), which is a nonsolvent for the pristine (oleate-capped) CQDs, and is immiscible with their original solvent (hexane). Ordered arrays were formed by slowly drying a small volume of the CQD dispersion injected onto an EG bath in a PTFE beaker covered with a glass slide; the schematics of the process steps are shown in **Figure 1(a)**. The obtained superlattices were used as-formed [referred to as oleic acid(OA)-capped samples], or after ligand exchange performed by injecting the ligand solution into the EG subphase.

In this study, we used tetrabutylammonium iodide (TBAI), ethanedithiol (EDT) and ethylenediamine (EDA), which are the most common ligands used in the field. The TBAI and EDT ligands are frequently used in the fabrication of electronically coupled lead-chalcogenide CQD solids due to their affinity to substitute the surface-bound oleate groups.^[20, 36-38] Instead, EDA is reported to remove lead-oleate from the surface.^[15, 39]

After ligand exchange, the films were transferred onto solid substrates by stamping, i.e. touching the liquid surface with a substrate kept parallel to the surface. This method results in highly ordered superlattices with domains as large as several hundred nanometers, as shown on the transmission electron microscope (TEM) image in Figure 1(b). Its Fourier-transformed version (see inset) indicates good ordering, and the typically observed lattice type is rhombic. Optical absorption of the superlattices was measured to learn about their degree of electronic coupling; the spectra normalized to the values at 1.2 eV are plotted on Figure 1(c). The properties of the as-prepared, OA-capped superlattices are remarkably similar to those of the original CQD solution. The first two excitonic transitions are observable as clear peaks around 0.8 and 1.0 eV, although they are less pronounced than in the isolated CQDs. The TBAI- and EDA-treated samples show similar peak positions to the OA-capped samples, with the latter exhibiting further decreased peak intensities. The lower peak intensity typically

originates from a changing oscillator strength stemming from an altered dielectric environment, or from a broadening due to inhomogeneous electronic coupling throughout the layer. The EDT-treated superlattices exhibit a red shift of about 50 meV of the first transition energy compared to the rest of the samples. Such behavior is often observed in thiol-treated CQD array due to the enhanced coupling caused by crosslinking and the related shrinking of the interparticle distance.^[36] Mild annealing of the EDA-treated samples lead to a further decrease in the excitonic peak intensity, which is typically sign of increased energetic disorder due to inhomogeneous coupling.

The local structure and symmetry of the superlattice and the orientation of the CQDs were investigated by transmission electron microscopy (TEM) and selected area electron diffraction (SAED). For clarity, all directions and indices are labeled with CQD (referring to the CQD crystal structure) or SL (referring to the superlattice geometry). In general, all samples show some degree of inhomogeneity in the extent and type of ordering; images from randomly selected spots on multiple samples were taken to obtain reliable statistics. Small area TEM images of representative close-packed areas of monolayer superlattice samples are shown on **Figure 2(a-d)**. All superlattices show an intermediate structure between hexagonal and square symmetries. The superlattice unit cell vectors were extracted from the fast Fourier-transformed (FFT) images by fitting to the peak positions. The lengths of the two lattice vectors and their angle (see scheme on panel i) obtained from numerous independent samples are summarized in Figure 2(j). The OA-capped samples show the lowest average angle of 70.1° , while values between 81.4 - 83.3° were measured for the three types of ligand-exchanged samples. The superlattice periodicity decreases from around 6.5 nm for the OA-capped samples to 5.8 nm for the EDA-treated ones. SAED patterns from highly ordered areas of the same samples are shown on panels (e-h). Dominant four-fold symmetry is observed in each SAED pattern; the peaks are the $\{100\}_{\text{CQD}}$ reflections, which are observed for PbSe single crystal seen in the $\langle 100 \rangle_{\text{CQD}}$ zone axis. The measured lattice parameters are

identical to the bulk values within the experimental error. Interestingly, the common orientation of the CQDs coexists with a lack of in-plane square symmetry in the superlattices; the neighboring CQDs are aligned, but their center is shifted (by 2-6 lattice planes in case of EDA, for example). The typical CQD orientational disorder varies between the samples. Azimuthal profiles of the first order peaks show Gaussian shape instead of a Lorentzian one, indicating that some CQDs are marginally misaligned. The Gaussian peak widths are shown on Figure 2(k); the orientation distribution narrows upon ligand exchange, and the best orientation is observed in the EDT- and EDA-treated samples.

Slightly different ordering is observed in multilayer superlattices. Representative FFT TEM images are shown in Figure S1 in the Supporting Information. In general, higher deviation in the lattice parameters, longer unit vectors and lower unit cell angles (with values around 73-75°) are observed in the ligand-exchanged multilayer superlattices, while the thick OA-capped samples are very similar to the monolayer ones. The unit cell angles of the OA-capped mono- and multilayers are close to what is expected from a body-centered cubic (BCC) superlattice seen from the $\langle 110 \rangle_{\text{SL}}$ zone axis. Such symmetry and orientation have been observed in lead-chalcogenide superlattices formed without ligand stripping.^[21, 28, 40] The thicker samples show symmetries close to a BCC structure even after ligand exchange. We also prepared a sample by drying a droplet of the CQD solution directly on the TEM grid, which gave close-to-hexagonal ordering with lattice spacing around 7 nm (Figure S1(g)); the presence of face-centered cubic lattices oriented with the $\langle 111 \rangle_{\text{SL}}$ zone axis normal to the substrate have also been observed, and are typical for spherical particles with isotropic interactions.^[28] The superlattice structure of the drop-cast OA-capped samples suggests that the orientation-specific interactions are not determining the superlattice symmetry under the applied conditions.^[16, 22] In fact, the same symmetry with lower interdot spacing is observed upon treating the drop-cast grids samples with an EDA solution, as shown on Figure S1(i).

On the other hand, initially a BCC lattice forms on the EG bath, likely due to the slower drying process.^[21] However, a large structural inhomogeneity is observed within and between samples without ligand treatment; the superlattice undergoes a slow transformation locally from BCC towards a simple cubic (SC) structure.^[22, 40] This process occurs through a subphase-mediated desorption of lead-oleate from the CQD surface, giving rise to an oriented attachment.^[11] These samples are mainly capped with oleate groups, but the ligand removal can occur easily from the $\{100\}_{\text{CQD}}$ facets, the ones with the lowest binding energy for oleate.^[19] The addition of reactive ligands assists this process through removing the oleate ligands that act as spacers. The exposure of the facets transforms the lattice, which is expected to appear as a change in the angle from $\sim 70^\circ$ to 90° , and a factor of $2^{1/3}$ decrease in the lattice parameter.^[40]

In our samples, the lower than 90° superlattice angles and a less pronounced decrease in the average superlattice spacing indicate that the transformation is not complete, which can be explained by a rapid stripping process leading to a very fast epitaxial necking and freezing of the structure, blocking the complete distortion of the superlattice. The differences between the mono- and multilayer sample lattice parameters in the ligand-treated samples suggest that the BCC-to-SC transformation is further hindered in a multilayer structure through out-of-plane stabilization by the shifted adjacent monolayers. This finding is supported by the similar structures of the OA-capped and EDA-treated drop-cast samples; when particles experience low rotational and translational freedom, the superlattice transformation remains partial, or does not occur at all. Nevertheless, the CQDs appear to be oriented with the $\langle 100 \rangle_{\text{CQD}}$ zone axis normal to the subphase surface in each superlattice sample, resulting in a hybrid structure. To understand the structural differences, one has to consider the ligand chemistry. All ligand treatments trigger the transformation of the superlattice, but the degree of ordering, especially at the atomic lattice level, is different. EG itself can strip the ligands,^[22] but it's inefficient, leading to a close-to-hexagonal structure. However, it can catalyze the exchange of oleate to

iodide,^[20] which leads to larger lattice transformation upon injection of TBAI. The similar chemistry is mainly responsible for the similar optical absorption spectra shown in Figure 1. On the other hand, EDT and EDA show distinctly different behavior; these highly reactive ligands induce some structural inhomogeneity. **Figure 3(a-d)** shows two pairs of images obtained from the EDT and EDA-treated superlattices, representing the two extremes of the spectrum of slightly different structures. One is similar to the OA-capped as-prepared samples (panels a and b), and the other is ligand-dependent (panels c and d). The inhomogeneity suggests that the ligand exchange is not occurring at the same rate around the whole sample; in some parts, the OA is only partially removed, while some parts show the very strong influence of the ligand. This inhomogeneity may be responsible for the similar peak positions in the absorbance spectra; the OA-like areas will exhibit similar features as the OA-capped samples, and the more coupled areas will give a broader peak with similar absorption at higher energies, causing an effective decrease in the peak position and intensity.

The difference in the ligand-specific structures in Figure 3(e,f) stems from the fundamentally different mechanism of the ligand exchange. EDT tends to attach to lead-chalcogenide CQDs by replacing the oleate ligands due to the high affinity of the thiol group to the lead-dominated surface.^[36, 41] The combined effect is an increase in the effective CQD size and the decrease in the superlattice spacing is observable in the absorption spectrum as a red-shift of the first excitonic peak. Interestingly, the particle shape in the extreme areas of the sample becomes more cubic, similar to what is occurring in sulfide-treated PbS CQDs.^[42-44] On the other hand, EDA removes lead-oleate groups, leaving a naked CQD behind.^[45, 46] The lower stability of the naked surfaces leads to restructuring by diffusion of surface atoms into the gap.^[16, 20] This way rather broad interparticle bridges, called necks, are formed between adjacent CQDs. Due to the decreasing CQD size and the positional disorder, many bridges simply don't form,^[7] resulting in the particular, semi-connected structure visible on Figure 3(d). Higher resolution images (panels e and f) confirm that the type of particle necking is

very different in the two systems. The EDT samples show many epitaxial connections, but the neck width is relatively small, only a few atoms in most cases. On the other hand, EDA results in fewer, but much broader necks, making the original shape of the QDs almost disappear.^[7, 31] From the HRTEM micrographs, it is possible to quantify the number and width of necks at the connection points. In the case of the EDT sample, we find that ~68% of the investigated connections are formed with an average neck width of 7 ± 2 atomic planes (see panel Figure 3(e) and Figure S2). On the other hand, only 53% of the connections are made using EDA, but the neck width in this sample increases to 10 ± 2 atomic planes, which is roughly 60% of the CQD diameter (see panel Figure 3(f) and Figure S2).

To complete the picture, the microscale morphology of the multilayer samples was investigated by AFM; examples of the micrographs are shown in Figure S3. We observe large flat areas of the multilayer films interrupted by micron-sized holes. The bottom of the holes is frequently covered with a monolayer. Both mono- and multilayer areas show RMS roughness ~ 1 nm indicating densely packed films, ruling out any significant cracking on this scale. Holes in larger number, but smaller in size are observed in the ligand-exchanged films compared to the OA-capped ones. A spin-coated reference was also prepared; the film is homogenous and flat, but shows a granular structure not present in the superlattice samples (Figure S3(d)).

To assess the relation between the structural and transport properties of the superlattices, we fabricated ion gel-gated field-effect transistors (IGFETs); the device structure is shown on the **Figure 4(a)**. For the purpose, we designed a device pattern of overall small channel areas in order to test as much as possible single superlattice domains: channels 1-10 μm long and 20 μm wide were used. Devices with different channel lengths were patterned close to each other to allow for contact resistance measurements (see panel b). For a proper statistics, several of these groups of devices were patterned on each substrate placed ~ 3 mm from each other. Rather thin, 30 nm electrodes were used to avoid major cracking upon film transfer. However,

the monolayer samples were found to be very fragile and reasonable channel coverage was only achieved using multilayer superlattices. After transferring the SL films onto the FET substrates, the samples were investigated with an optical microscope and only the devices with (visibly) full coverage and without macroscopic cracks were characterized.

Figure 4(c) shows the typical transfer curves measured in the four different sample types. Independently from the ligand, all samples show electron-dominated ambipolar characteristics previously observed in many lead-chalcogenide CQD FETs.^[3, 20, 29, 34] Applying positive gate voltages, the samples show practically no hysteresis, but degrade rapidly under negative gate bias, resulting in a huge hysteresis loop. The degradation is visible as the CQD film breaks up and disappears, and is possibly caused by dissolution of the CQDs in the electrolyte.^[47] The gate current is orders of magnitude below the source and drain currents in the n-channel, but the values are comparable in the p-channel (Figure S4(a)); thus, for the sake of reliability, we focus only on the electron transport. Figure 4(d-e) reports textbook-like output and transfer characteristics for the EDA treated sample, similar behavior is obtained for the others samples as well. All devices show good electron transport with linear dependence of the current at high gate voltages (sign of operation in the linear regime), “on” currents of several μA , and “off” currents in the nA range. The on/off ratio usually exceeds 10^3 , and reaches $>10^4$ in the best samples, indicating significantly retained quantum confinement. These values are limited by the relatively low channel aspect ratio and the consequent low ‘on’ current, and the relatively high Faradaic gate leakage that sets the value of the “off” state current. We observe a transient behavior during the first few gate scans; although the slope of the linear part of the curves is similar, the intercept shifts to lower values, which causes an increase in the maximum “on” current within the given voltage window. The constant slope indicates that the mobility is unchanged, but the changing intercept indicate a threshold shift, likely through gate-induced removal or addition of trapped charges. Stable behavior is reached after

switching the devices on and off twice (see Figure S4(b)), requiring a “warm-up” of the each device before achieving stable and reproducible measurements.

Although the general device characteristics of samples fabricated with different ligands are very similar, we observe a striking, magnitude difference in the “on” state current between the EDA-treated films and the rest of the samples.

Field-effect electron mobilities were calculated from the transfer curves using the gradual channel approximation in the linear regime. The data are plotted on Figure 4(f) in three groups: EDA-treated superlattice, EDA-treated spin-coated film and the rest of the superlattice samples. The values of the mobility, for different channel dimensions and the distribution per substrate are listed in Table S1. The mobility values show large variation, spanning almost an order of magnitude for each sample type. No clear difference is observable between the OA-capped, the TBAI- and the EDT-treated samples (noted as SL-other), while superlattice devices prepared using EDA (referred to as SL-EDA) show much higher mobilities. An average electron mobility of $13 \text{ cm}^2/\text{Vs}$ was found for EDA, against the $4.9 \text{ cm}^2/\text{Vs}$ for the rest of the superlattice samples. The mobilities reported for SL-EDA samples are obtained from two substrates, as shown by the different colors on Figure 4(f), with average mobility of 12 and $15 \text{ cm}^2/\text{Vs}$. The values obtained for the non-EDA superlattices are comparable to those reported by Alimoradi Jazi *et al.*,^[33] while the EDA-based ones (averaged on either substrate) are the highest ever reported for quantum confined lead-chalcogenide superlattice samples.

We compared these results with values obtained from a spin-coated reference sample treated with EDA (see fabrication details in the Supporting Information). The spin-coated devices (labeled as SP-EDA) do not compete in mobility with the EDA superlattice layers, but give values similar to the ones prepared with the other ligands, with an average of $3.8 \text{ cm}^2/\text{Vs}$.

At this point is important to underline that several measures were taken to ensure the reliability of the calculated mobility values. The channel lengths were determined using AFM,

and were found slightly lower than the intended values; the measured data were used for calculation to avoid overestimation of the mobility. The ion-gel capacitance was measured in similar conditions to the transfer curve measurements. Several electrode pairs with different areas were measured to correct for the different size of the top and bottom electrodes, and an average value of the single layer capacitance was used for the mobility calculation (see more in the Supporting Information).^[43] The main factors that can result in overestimation of the mobility, such as using too low capacitance or too short channel length are excluded by measurements. Some factors that cause underestimation, for example cracks and holes in the layers, are not corrected for in the dataset presented on Figure 4(f), and thus the data can be considered as conservative estimates of the sample mobility.

Making use of the adjacent devices with different channel lengths, we estimated the contact resistance using the transfer line method (see the details in the Supporting Information). The obtained values (2-3 k Ω) are significant compared to the channel resistance in the shortest devices (Figure S5), thus a correction for the voltage drop is required. We calculated a contactless mobility of 19.1 and 24.2 cm²/Vs for the two datasets used in the TLM calculations, 10-80% higher than the values from single device transfer curves, depending on the channel length and the corresponding relative potential drop at the contacts. These are average values for an area on the 100 μ m scale, and are the highest reported for lead-chalcogenide CQDs. The results demonstrate, especially compared to ref 24, that chemically triggered ligand desorption is more effective in achieving high carrier mobilities than a thermal trigger.

However, two concerns rise when analyzing the data: why do the EDA-based superlattices perform so well in FETs compared to the EDT ones despite the similar superlattice structure, and why do we observe such large variation in the mobility values? Before measuring the FETs, we ensured that the electrodes and the channel area are covered by flakes of the superlattice, without macroscopic cracks. Based on the similarity in the substrate coverage

calculated from the AFM images (92 % for the EDT-treated sample and 95% for the EDA-treated one), we rule out a strong, trend-wise influence of 0.1-1 micron scale cracks in the films. Consequently, the difference must lie in the structural details at the nanoscale. The first point can be explained by the CQD connections in the samples; the number and width of epitaxial necks are distinctly different in the EDT- and EDA-treated superlattices as shown in Figure 3(e-f), due to the different chemical behavior of EDT and EDA. The type and density of necking being the largest difference in the two structures, our data suggests that transport through the non-linear, percolative pathways is much more efficient than transport through a highly ordered, homogeneous, but more confined, and therefore electronically less coupled array. This finding confirms that high coupling through epitaxial necking is needed between the adjacent dots to achieve efficient transport over a large distance. The second point can be resolved by considering the observed inhomogeneity in the samples. The regions that are more alike to the OA-capped samples shown on Figure 3(a,c) will likely exhibit lower charge carrier mobility than the percolative regions on Figure 3(d), following the arguments on the importance of the neck width.^[7] The BCC- and SC-like regions in the OA-capped samples are also expected to give different transport properties due to the different interdot spacing. Moreover, the number and density of the holes and cracks in the films will strongly affect the observed mobilities. The difference between the spin-coated and superlattice EDA samples can also be explained by the morphology; the granular structure of the spin-coated sample does not provide the long, uninterrupted pathways for charge transport present in the percolative superlattices.^[31]

Although the results show large variation, and improvements in the fabrication process are clearly necessary to fabricate more homogeneous samples and reproducible devices, the measured mobility values show the great prospects of lead-chalcogenide superlattices. It is important to mention that despite the different scales of the measurements (0.1-1 micron for TEM, 1-100 micron for FET and 1 mm for absorbance), the data were obtained from different

locations of several mm sized samples, indicating that the structural and transport properties describe a system that shows quantum confinement, and the high mobilities were achieved despite the presence of electronic disorder.^[7] This dual behavior gives the prospects of achieving true freedom in the engineering of electronic and optical properties in these fascinating materials. As a final note, tuning of the annealing conditions leads to mobilities above 40 cm²/Vs, therefore an increased control of the process may lead to unexpected results for CQD superlattices.

Conclusion

In conclusion, we compared the nanostructure and the electrical transport properties of PbSe CQD superlattices formed using different ligands. The symmetry of the superlattice depends on the applied ligand, allowing for tuning the charge transport properties. Two-contact electron mobilities with an average of 13 cm²/Vs for small area superlattice FETs prepared using EDA are measured. From these devices, we derive contactless mobilities up to 24 cm²/Vs using the transfer line method. Such high values have not been reported in low-temperature processed CQD devices, and are comparable to those reported for heavy sintering. Importantly, the electron mobility in the superlattice samples is almost an order magnitude higher than in samples fabricated using the conventional layer-by-layer spin-coating method. Furthermore, we demonstrated that the width and not the density and homogeneity of the interparticle connections determines the efficiency of the charge transport. The achieved high mobility in ordered structures is the first clear experimental evidence of the potential of colloidal QD superlattices for optoelectronics. The challenges and difficulties of the fabrication process show the direction towards further improvements in the electronic properties of these fascinating materials.

Experimental Section

Chemicals: Lead (II) acetate trihydrate (99.999%), 1-octadecene (ODE, 90%), oleic acid (OA, 90%), tributylphosphine (TBP, 97%), selenium shots (99.99%), tetrabutylammonium iodide (TBAI, >99.0%), ethylenediamine (EDA, >99.0%), ethanedithiol (EDT, >98.0%), ethylene glycol (EG, 99.8%, anh.), ethanol (anh.), hexanes (>99.0%, anh.) and acetonitrile (99.8%, anh.) were purchased from Aldrich. All chemicals were used as received. All syntheses were carried out using standard airless techniques: a vacuum/dry nitrogen gas. Schlenk line was used for NPs syntheses and a nitrogen glove-box for storing and handling air and moisture-sensitive chemicals and CQD purification.

PbSe CQD synthesis: Monodisperse PbSe CQDs were prepared similarly to a previously reported procedure by Wang *et al.*^[48] In a typical synthesis, Pb(OAc)₂·3H₂O (1.338 g, 4.1 mmol) and oleic acid (4.5 ml OA) were mixed in 10 ml of octadecene. This mixture was degassed at room temperature, 50 °C, 70 °C, 90 °C and 110 °C for 10 minutes each to form the lead oleate complex. The solution was flushed with nitrogen, and the temperature was raised to the reaction temperature (160 °C). At this temperature, Se precursor (10 ml, 1M), prepared by dissolving selenium shots in TBP was rapidly injected. The reaction mixture was maintained ca. 160 °C for 30 seconds and then quickly cooled down to room temperature using a water bath. The formed PbSe CQDs were thoroughly washed in inert atmosphere by 3 precipitation/redispersion steps using anhydrous ethanol as a non-solvent and anhydrous hexane as a solvent. Finally, the CQDs were dispersed in anhydrous hexane with a concentration of 50 mg/ml, and optical absorption was performed to determine the CQD size (5.2 nm according to the sizing curve of Moreels *et al.*) and quality of the batch.^[49]

Superlattice fabrication: The fabrication process was based on the methods described by Dong *et al.* and Whitham *et al.*^[7, 10, 12] For the superlattice formation, 1.5 mL ethylene glycol was poured in a 1.5×1.5×1.5 cm Teflon well set up in a glovebox filled with dry nitrogen (<0.1 ppm O₂/H₂O). The given amount of the CQD sol (2.5 mgmL⁻¹ in hexanes, 2.5μL for monolayers, 5μL for multilayers) was injected on top of the bath, and the well was

immediately covered by a glass slide. After 20 min, 5 μL of a 1 M ligand solution in acetonitrile was injected into the bottom of the well, and the system was let to react for 2-3 minutes under cover. The films were transferred by touching the liquid surface with a substrate/grid, and the samples were dried for at least 3 hours in mbar vacuum.

Structural and optical characterization: The absorption spectra were obtained with a Shimadzu UV3600 spectrometer. JEOL 2010 and 2010F transmission electron microscopes were used for the structural characterization. The superlattice unit cells were determined from 600x600 nm regions by fitting two vectors to the peak positions extracted from the Fourier-transformed images. The atomic lattice vectors were extracted following the same method from the SAED patterns measured at 130 nm diameter areas. The AFM images were delivered by a WiTec Alpha SNOM-AFM operated in contact mode.

FET fabrication and characterization: Sets of devices were patterned onto borosilicate glass using UV photolithography, and 30 nm Pt electrodes were deposited by sputtering. The substrates were cleaned by soap, water, acetone and isopropanol, and were annealed at 120°C inside a glovebox right before film deposition. The substrates were cleaned by soap, acetone and isopropanol, and were annealed at 120°C inside a glovebox right before film deposition. The spin-coated reference sample was fabricated by spinning a 2.5 mg mL^{-1} solution on a substrate, flooding the film with a 20 mM EDA solution in acetonitrile, and the process was repeated once to fill the cracks and achieve similar thickness to the superlattices. The ion gel was prepared following a literature recipe.^[50] The FET samples were annealed at 120°C for 20 minutes to remove all adsorbed species,^[51] the ion gel was dropped on the films leaving the electrode contact pads uncovered, and the samples were dried at 70 °C overnight. A piece of platinum foil placed on top of the gel-covered devices was used as gate electrode, and a platinum wire was stick into the gel to measure the reference potential. The FETs were characterized using an Agilent E5270B semiconductor parameter analyzer in inert

environment. The ion gel impedance was obtained using a BioLogic SP200 potentiostat in vacuum (details can be found in the Supporting Information).

Supporting Information

Supporting Information is available from the Wiley Online Library or from the author.

Acknowledgements

M.A.L, D.M.B and A.G.S are grateful for the financial support of the European Research Council via a Starting Grant (HySPOD, No. 306983). M.V.K. acknowledges partial financial support from the European Union (EU) via FP7 ERC Starting Grant 2012 (Project NANOSOLID, GA No. 306733). M.I. was supported by AGAUR via Beatriu i Pinós fellowship and by ETH Zurich via ETH career seed grant (SEED-18 16-2). B.M.M. is recipient of the Tata Steel Scholarship at the University of Groningen.

Received: ((will be filled in by the editorial staff))

Revised: ((will be filled in by the editorial staff))

Published online: ((will be filled in by the editorial staff))

References

- [1] M. Liu, O. Voznyy, R. Sabatini, García De Arquer, F. Pelayo, R. Munir, A. H. Balawi, X. Lan, F. Fan, G. Walters, A. R. Kirmani, S. Hoogland, F. Laquai, A. Amassian, E. H. Sargent, *Nat. Mater.* **2017**, *16*, 258.
- [2] J. H. Choi, H. Wang, S. J. Oh, T. Paik, P. Sung, J. Sung, X. Ye, T. Zhao, B. T. Diroll, C. B. Murray, C. R. Kagan, *Science* **2016**, *352*, 205.
- [3] A. G. Shulga, V. Derenskyi, J. M. Salazar Rios, D. N. Dirin, M. Fritsch, M. V. Kovalenko, U. Scherf, M. A. Loi, *Adv. Mater.* **2017**, *29*, 1701764.
- [4] J. Schornbaum, Y. Zakharko, M. Held, S. Thiemann, F. Gannott, J. Zaumseil, *Nano Lett.* **2015**, *15*, 1822.
- [5] D. V. Talapin, J. Lee, M. V. Kovalenko, E. V. Shevchenko, *Chem. Rev.* **2010**, *110*, 389.
- [6] C. R. Kagan, E. Lifshitz, E. H. Sargent, D. V. Talapin, *Science* **2016**, *353*, 885.
- [7] K. Whitham, J. Yang, B. H. Savitzky, L. F. Kourkoutis, F. Wise, T. Hanrath, *Nat. Mater.* **2016**, *15*, 557.
- [8] D. Vanmaekelbergh, P. Liljeroth, *Chem. Soc. Rev.* **2005**, *34*, 299.

- [9] C. B. Murray, C. R. Kagan, M. G. Bawendi, *Science* **1995**, 270, 1335.
- [10] A. Dong, J. Chen, P. M. Vora, J. M. Kikkawa, C. B. Murray, *Nature* **2010**, 466, 474.
- [11] W. H. Evers, B. Goris, S. Bals, M. Casavola, J. de Graaf, R. van Roij, M. Dijkstra, D. Vanmaekelbergh, *Nano Lett.* **2013**, 13, 2317.
- [12] A. Dong, Y. Jiao, D. J. Milliron, *ACS Nano* **2013**, 7, 10978.
- [13] M. P. Boneschanscher, W. H. Evers, J. J. Geuchies, T. Altantzis, B. Goris, F. T. Rabouw, S. A. van Rossum, van der Zant, H. S., L. D. Siebbeles, G. Van Tendeloo, I. Swart, J. Hilhorst, A. V. Petukhov, S. Bals, D. Vanmaekelbergh, *Science* **2014**, 344, 1377.
- [14] R. Sharma, A. M. Sawvel, B. Barton, A. G. Dong, R. Buonsanti, A. Llodes, E. Schaible, S. Axnanda, Z. Liu, J. J. Urban, D. Nordlund, C. Kisielowski, D. J. Milliron, *Chem. Mater.* **2015**, 27, 2755.
- [15] W. Walravens, J. De Roo, E. Drijvers, S. Ten Brinck, E. Solano, J. Dendooven, C. Detavernier, I. Infante, Z. Hens, *ACS Nano* **2016**, 10, 6861.
- [16] D. Li, M. H. Nielsen, J. R. Lee, C. Frandsen, J. F. Banfield, J. J. De Yoreo, *Science* **2012**, 336, 1014.
- [17] W. J. Baumgardner, K. Whitham, T. Hanrath, *Nano Lett.* **2013**, 13, 3225.
- [18] S. J. Oh, N. E. Berry, J. H. Choi, E. A. Gaulding, H. Lin, T. Paik, B. T. Diroll, S. Muramoto, C. B. Murray, C. R. Kagan, *Nano Lett.* **2014**, 14, 1559.
- [19] D. Zhrebetskyy, M. Scheele, Y. Zhang, N. Bronstein, C. Thompson, D. Britt, M. Salmeron, P. Alivisatos, L. W. Wang, *Science* **2014**, 344, 1380.
- [20] D. M. Balazs, D. N. Dirin, H. Fang, L. Protesescu, G. H. ten Brink, B. J. Kooi, M. V. Kovalenko, M. A. Loi, *ACS Nano* **2015**, 9, 11951.
- [21] M. C. Weidman, D. M. Smilgies, W. A. Tisdale, *Nat. Mater.* **2016**, 15, 775.
- [22] J. J. Geuchies, C. Van Overbeek, W. H. Evers, B. Goris, A. De Backer, A. P. Gantapara, F. T. Rabouw, J. Hilhorst, J. L. Peters, O. Konovalov, A. V. Petukhov, M. Dijkstra, L. D. A. Siebbeles, S. Van Aert, S. Bals, D. Vanmaekelbergh, *Nat. Mater.* **2016**, 15, 1248.
- [23] D. V. Talapin, C. B. Murray, *Science* **2005**, 310, 86.
- [24] T. Hanrath, D. Veldman, J. J. Choi, C. G. Christova, M. M. Wienk, R. A. J. Janssen, *ACS Appl. Mater. Interfaces* **2009**, 1, 244.
- [25] J. J. Choi, C. R. Bealing, K. Bian, K. J. Hughes, W. Zhang, D. Smilgies, R. G. Hennig, J. R. Engstrom, T. Hanrath, *J. Am. Chem. Soc.* **2011**, 133, 3131.
- [26] H. Zhang, B. Hu, L. Sun, R. Hovden, F. W. Wise, D. A. Muller, R. D. Robinson, *Nano Letters* **2011**, 11, 5356.

- [27] C. S. S. Sandeep, J. M. Azpiroz, W. H. Evers, S. C. Boehme, I. Moreels, S. Kinge, L. D. A. Siebbeles, I. Infante, A. J. Houtepen, *ACS Nano* **2014**, *8*, 11499.
- [28] M. Weidman, K. Yager, W. Tisdale, , *Chemistry of Materials* **2014**, *27*, 474.
- [29] S. J. Oh, Z. Wang, N. E. Berry, J. H. Choi, T. Zhao, E. A. Gaulding, T. Paik, Y. Lai, C. B. Murray, C. R. Kagan, *Nano Lett.* **2014**, *14*, 6210.
- [30] M. Cargnello, A. C. Johnston-Peck, B. T. Diroll, E. Wong, B. Datta, D. Damodhar, V. V. T. Doan-Nguyen, A. A. Herzing, C. R. Kagan, C. B. Murray, *Nature* **2015**, *524*, 450.
- [31] W. H. Evers, J. M. Schins, M. Aerts, A. Kulkarni, P. Capiod, M. Berthe, B. Grandidier, C. Delerue, Zant, Herre S J van der, C. v. Overbeek, J. L. Peters, D. Vanmaekelbergh, L. D. A. Siebbeles, *Nat. Commun.* **2015**, *6*, 9195.
- [32] M. Zhao, F. Yang, C. Liang, D. Wang, D. Ding, J. Lv, J. Zhang, W. Hu, C. Lu, Z. Tang, *Adv. Funct. Mater.* **2016**, *26*, 5182.
- [33] M. Alimoradi Jazi, V. A. E. C. Janssen, W. H. Evers, A. Tadjine, C. Delerue, L. D. A. Siebbeles, H. S. J. van der Zant, A. J. Houtepen, D. Vanmaekelbergh, *Nano Lett.* **2017**, *17*, 5238.
- [34] Y. Liu, J. Tolentino, M. Gibbs, R. Ihly, C. L. Perkins, Y. Liu, N. Crawford, J. C. Hemminger, M. Law, *Nano Lett.* **2013**, *13*, 1578.
- [35] V. Sayevich, N. Gaponik, M. Plötner, M. Kruszynska, T. Gemming, V. M. Dzhagan, S. Akhavan, D. R. T. Zahn, H. V. Demir, A. Eychemüller, *Chem. Mater.* **2015**, *27*, 4328.
- [36] J. M. Luther, M. Law, Q. Song, C. L. Perkins, M. C. Beard, A. J. Nozik, *ACS Nano* **2008**, *2*, 271.
- [37] D. Zhitomirsky, M. Furukawa, J. Tang, P. Stadler, S. Hoogland, O. Voznyy, H. Liu, E. H. Sargent, *Adv. Mater.* **2012**, *24*, 6181.
- [38] A. G. Shulga, L. Piveteau, S. Z. Bisri, M. V. Kovalenko, M. A. Loi, *Adv. Electron. Mater.* **2016**, *2*, 1500467.
- [39] M. Law, J. M. Luther, O. Song, B. K. Hughes, C. L. Perkins, A. J. Nozik, *J. Am. Chem. Soc.* **2008**, *130*, 5974.
- [40] K. Whitham, T. Hanrath, *J. Phys. Chem. Lett.* **2017**, *8*, 2623.
- [41] M. S. Kang, A. Sahu, D. J. Norris, C. D. Frisbie, *Nano Lett.* **2011**, *11*, 3887.
- [42] H. Zhang, J. Yang, T. Hanrath, F. W. Wise, *Phys. Chem. Chem. Phys.* **2014**, *16*, 14640.
- [43] D. M. Balazs, K. I. Bijlsma, H. Fang, D. N. Dirin, M. Döbeli, M. V. Kovalenko, M. A. Loi, *Sci. Adv.* **2017**, *3*, eaao1558.
- [44] B. E. Trembl, B. H. Savitzky, A. M. Tirmzi, J. C. DaSilva, L. F. Kourkoutis, T. Hanrath, *ACS Appl. Mater. Interfaces* **2017**, *9*, 13500.

- [45] C. S. S. Sandeep, J. M. Azpiroz, W. H. Evers, S. C. Boehme, I. Moreels, S. Kinge, L. D. A. Siebbeles, I. Infante, A. J. Houtepen, *ACS Nano* **2014**, *8*, 11499.
- [46] E. Drijvers, J. De Roo, J. C. Martins, I. Infante, Z. Hens, *Chem.Mater.* **2018**, *30*, 1178.
- [47] H. Zhang, K. Dasbiswas, N. B. Ludwig, G. Han, B. Lee, S. Vaikuntanathan, D. V. Talapin, *Nature* **2017**, *542*, 328.
- [48] R. Y. Wang, J. P. Feser, J. Lee, D. V. Talapin, R. Segalman, A. Majumdar, *Nano Lett.* **2008**, *8*, 2283.
- [49] I. Moreels, K. Lambert, D. De Muynck, F. Vanhaecke, D. Poelman, J. C. Martins, G. Allan, Z. Hens, *Chem. Mater.* **2007**, *19*, 6101.
- [50] K. H. Lee, M. S. Kang, S. Zhang, Y. Gu, T. P. Lodge, C. D. Frisbie, *Adv. Mater.* **2012**, *24*, 4457.
- [51] D. M. Balazs, M. I. Nugraha, S. Z. Bisri, M. Sytnyk, W. Heiss, M. A. Loi, *Appl. Phys. Lett.* **2014**, *104*, 112104.

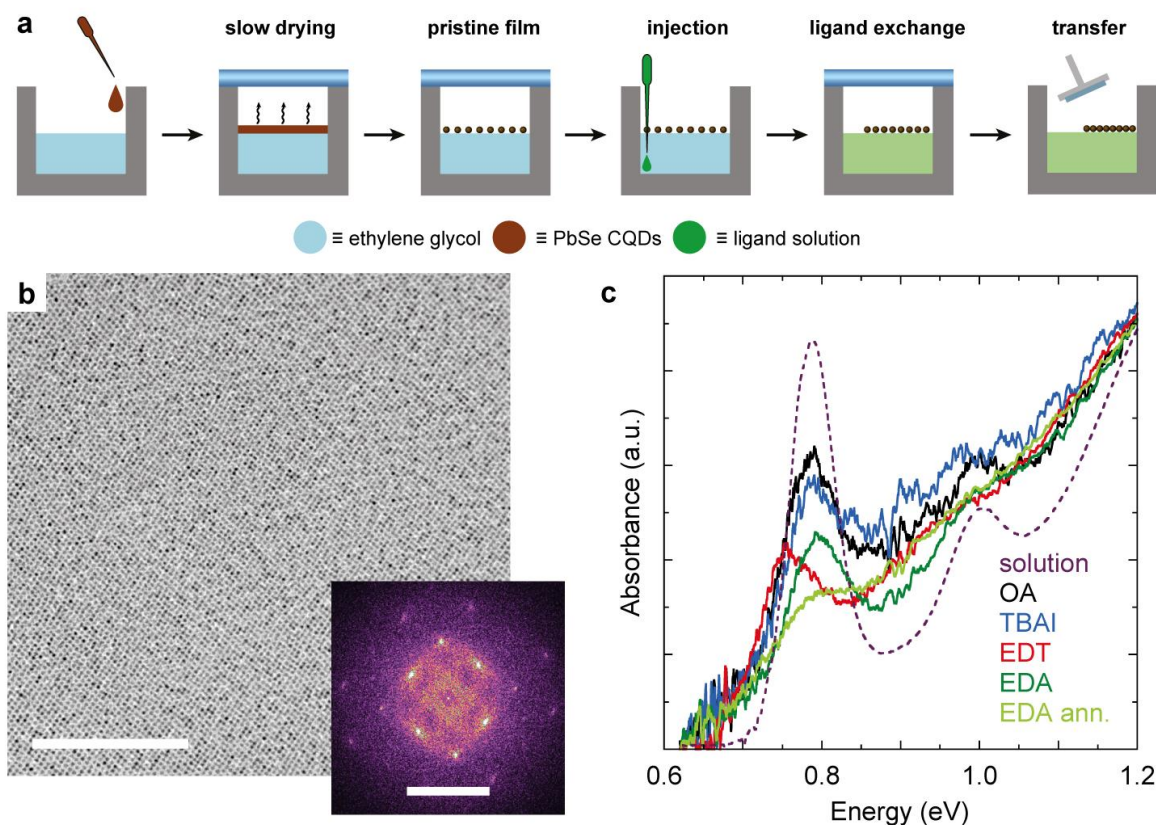


Figure 1. (a) Schematic of the sample fabrication based on the formation of an ordered PbSe CQD array on the surface of a nonsolvent and subsequent ligand exchange, details of the process are found in the main text; (b) TEM image and its fast-Fourier-transformed version (inset) of a sample prepared using EDA ligand solution showing a micron-sized superlattice domain with good ordering (the scale bars are 200 nm and 0.3 nm⁻¹ in the main figure and inset, respectively); (c) normalized absorption spectra of the CQDs in hexane, the formed superlattices and the EDA-based sample after annealing showing the presence of quantum confinement.

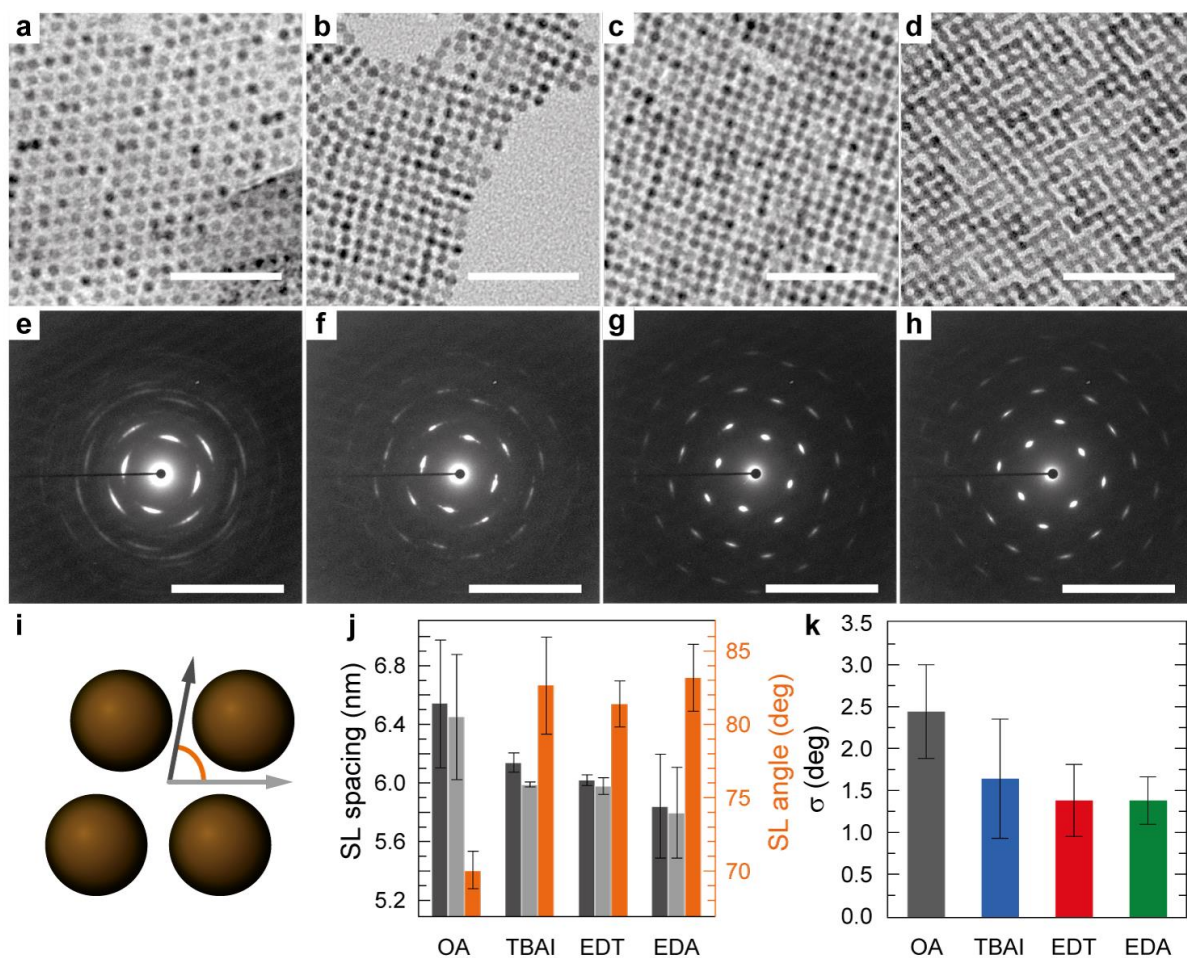


Figure 2. Structure of PbSe CQD superlattice samples: (a-d) representative TEM images of the superlattices with OA, TBAI, EDT and EDA ligands, respectively (scale bars 50 nm); (e-h) SAED patterns obtained from highly ordered domains of the same samples (scale bars 10 nm⁻¹); (i) scheme of the superlattice unit cell; (j) superlattice spacing and angle obtained from the FFT TEM images for the different ligands averaged over several samples and regions, the error bars represent the 95% confidence interval, the colors match those used on panel i; (k) Gaussian peak width of the azimuthal cross-section of the first order peaks extracted from the SAED patterns, the error bars represent the standard deviation of the values over the four corresponding peaks.

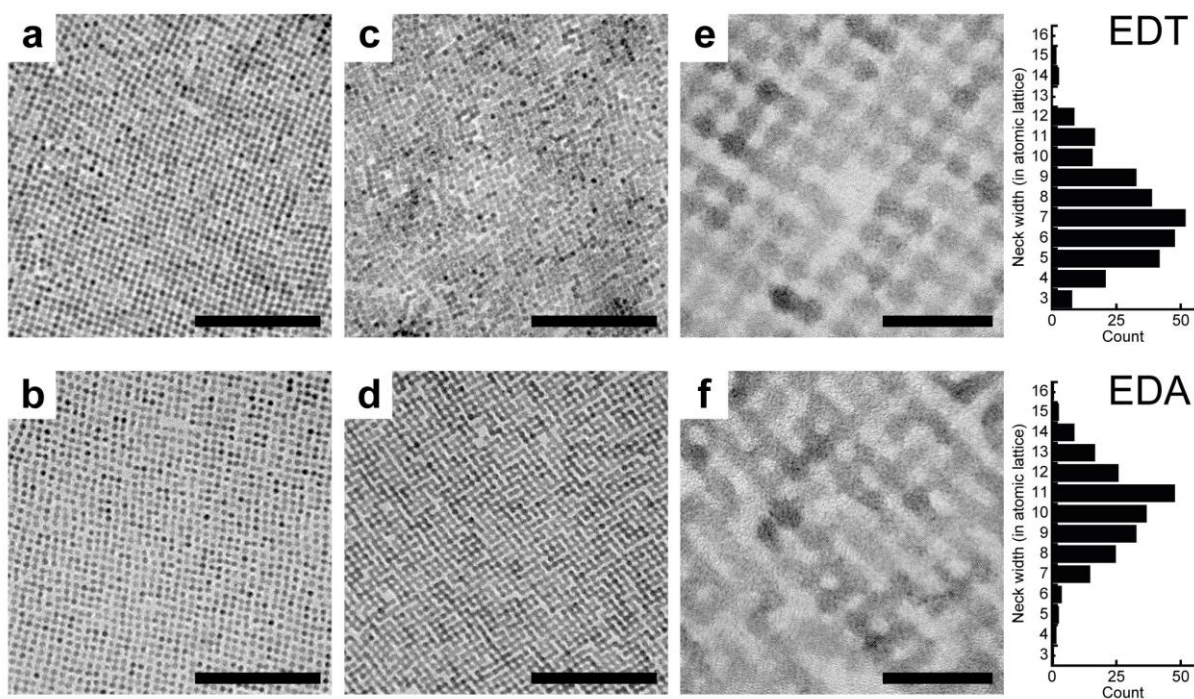


Figure 3. TEM images of different superlattice structures formed by treatment with EDT (top row) and EDA (bottom row) showing the sample inhomogeneity: (a,b) less connected and (c,d) more connected regions as the two extremes on a spectrum of structures obtained; (e,f) higher magnification TEM images of EDT and EDA-treated superlattices showing the difference in necking, and the histograms of the connectivity statistics collected from >200 CQDs (>400 connections) in each case. The scale bars are 100 nm (a-d) and 20 nm (e,f).

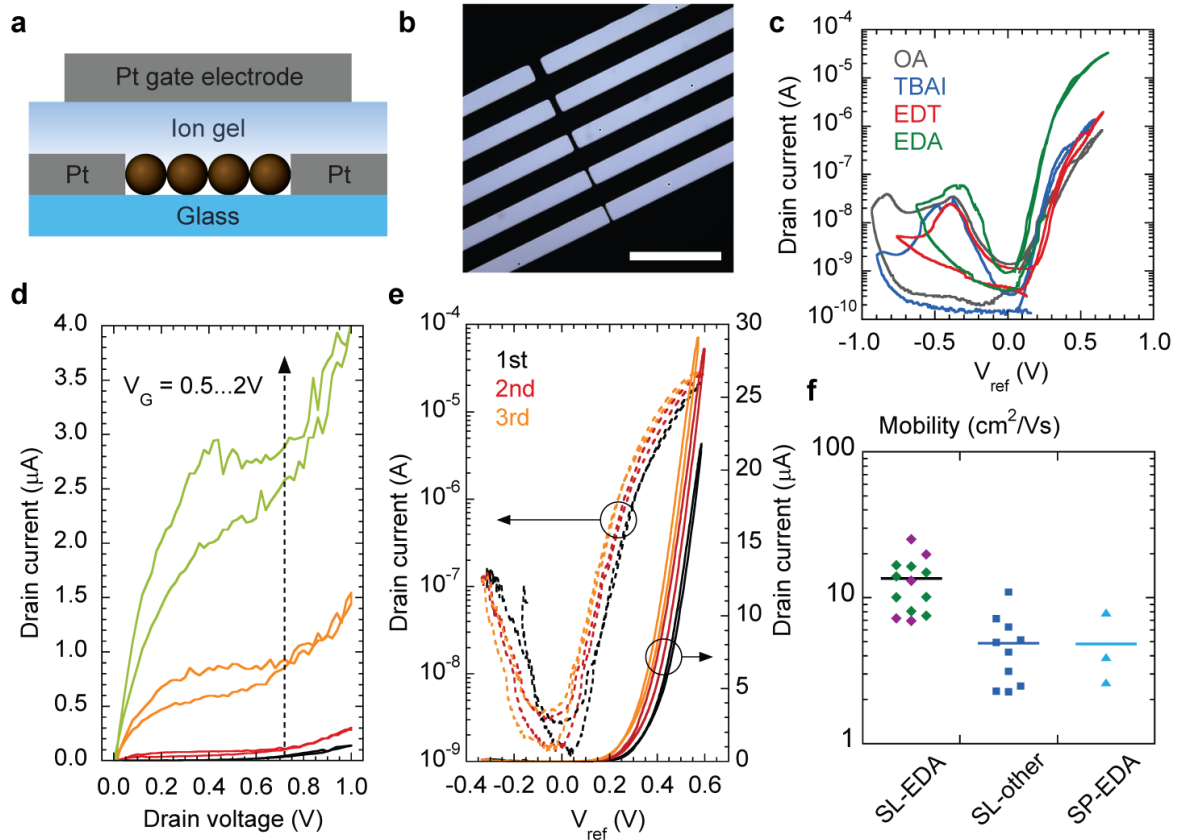


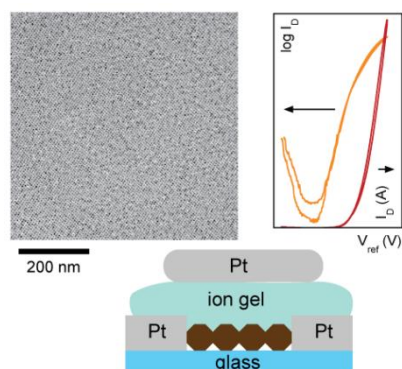
Figure 4. Field effect transistors based on PbSe CQD superlattices: a) device structure; b) micrograph of a set of devices; c) representative transfer curves of 5 μm channel length devices measured at 0.1 V drain bias; (d) output curves of a 2 μm channel length FET prepared using EDA; (e) transfer curves of a 2 μm channel length FET prepared using EDA, showing stable slope, but shifting intercept upon multiple scans; (f) statistics of the calculated electron mobilities; SL – superlattice, SP – spin-coated film, the different colors for the SL-EDA data indicate devices on the same substrate.

Colloidal quantum dot superlattices carry the promise of facile tuning the electronic structure of the assembly through engineering the interdot interactions. Balancing between quantum confinement and electronic coupling is possible through fine-tuning the layer structure through the conditions of the self-assembly and the layer stabilization process. This flexibility in the properties is highly important for novel optoelectronic applications.

Colloidal quantum dot superlattices

Dr. D. M. Balazs, B. M. Matysiak, Dr. J. Momand, A. G. Shulga, Dr. M. Ibáñez, Prof. M. V. Kovalenko, Prof. B. J. Kooi, Prof M.A. Loi*

Electron mobility of 24 cm²/Vs in PbSe colloidal quantum dot superlattices



Supporting Information

Electron mobility of 24 cm²/Vs in PbSe colloidal quantum dot superlattices

*Daniel M. Balazs, Bartosz M. Matysiak, Jamo Momand, Artem G. Shulga, Maria Ibáñez, Maksym V. Kovalenko, Bart J. Kooi, Maria Antonietta Loi**

E-mail: m.a.loi@rug.nl

Additional figures

- Figure S1. Structure of the multilayer samples
- Figure S2. Neck width statistics using EDT and EDA
- Figure S3. AFM images of the different films
- Figure S4. Additional FET data
- Table S1. List of measured mobility values

Contact resistance and contactless mobility calculation

Ion-gel characterization

Additional figures

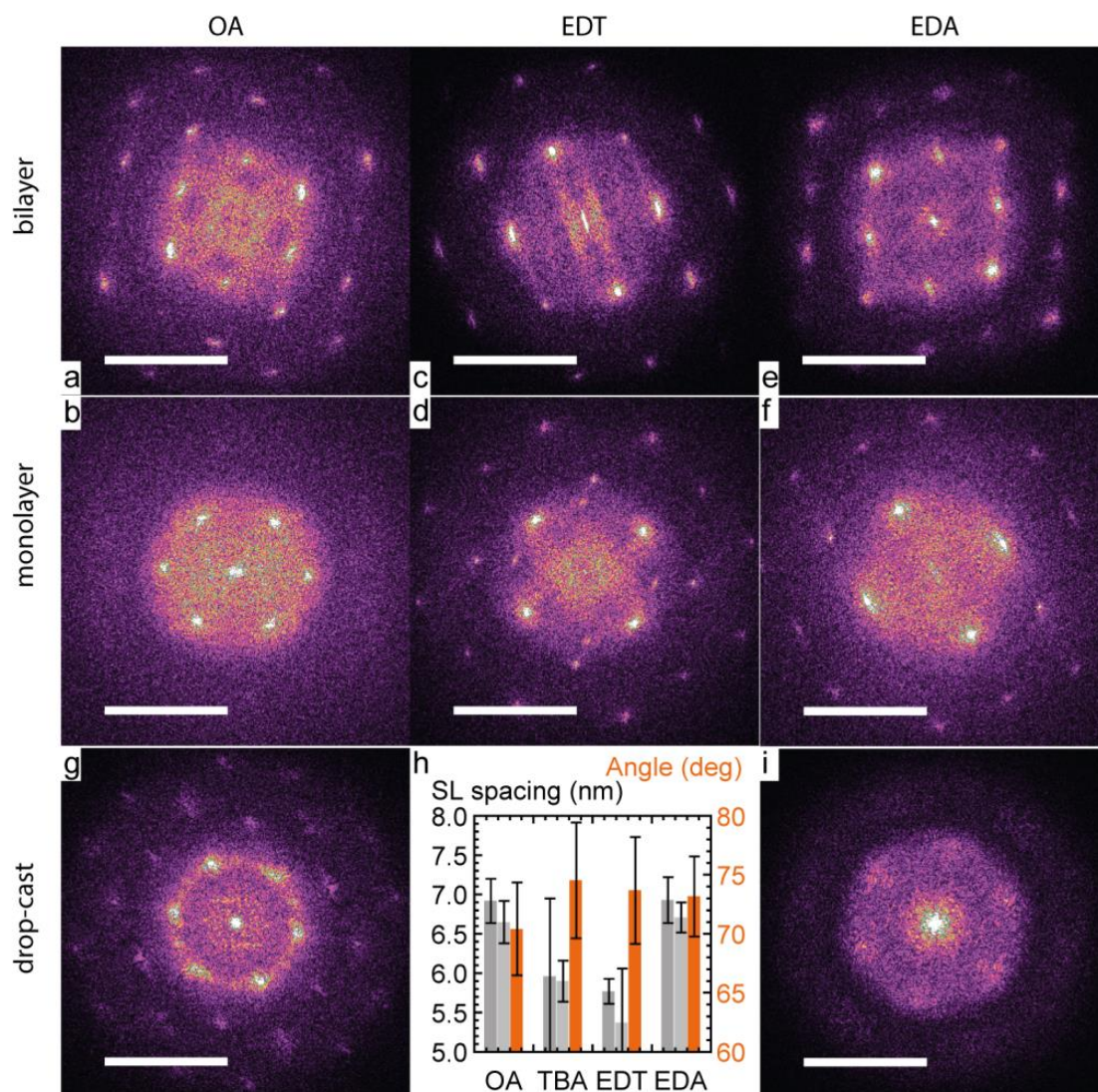


Figure S1. Fast-Fourier-transformed TEM images of (a,c,e) bilayer and (b,d,f) monolayer superlattices, and (g,i) drop-cast samples using (a,b,g) OA, (c,d) EDT and (e,f,i) EDA ligands, the scale bars are 0.3 nm^{-1} ; (h) extracted lattice parameters for bilayer superlattices.

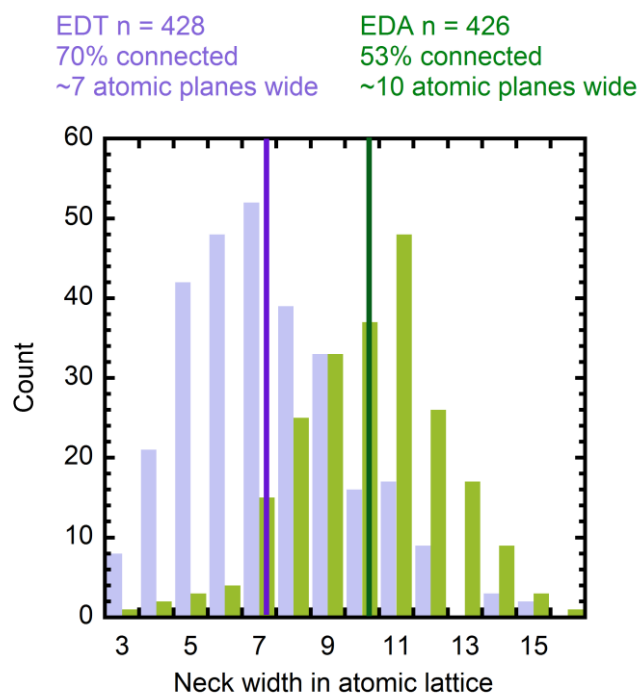


Figure S2. Quantification of the neck width in EDT- and EDA-treated superlattices, the statistic is reporting more than 400 necks for both samples, the two lines indicate the average of the 2 distributions.

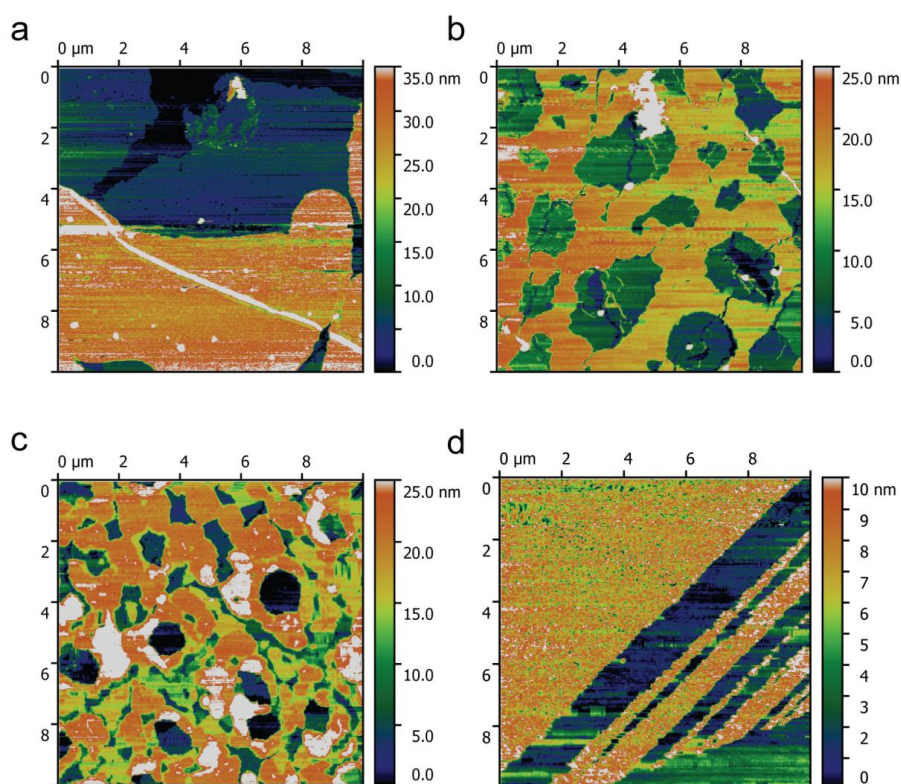


Figure S3. AFM images of superlattices formed using a) OA, b) EDT and c) EDA ligand, and d) image of the spin-coated reference sample showing a more homogeneous, but granular structure.

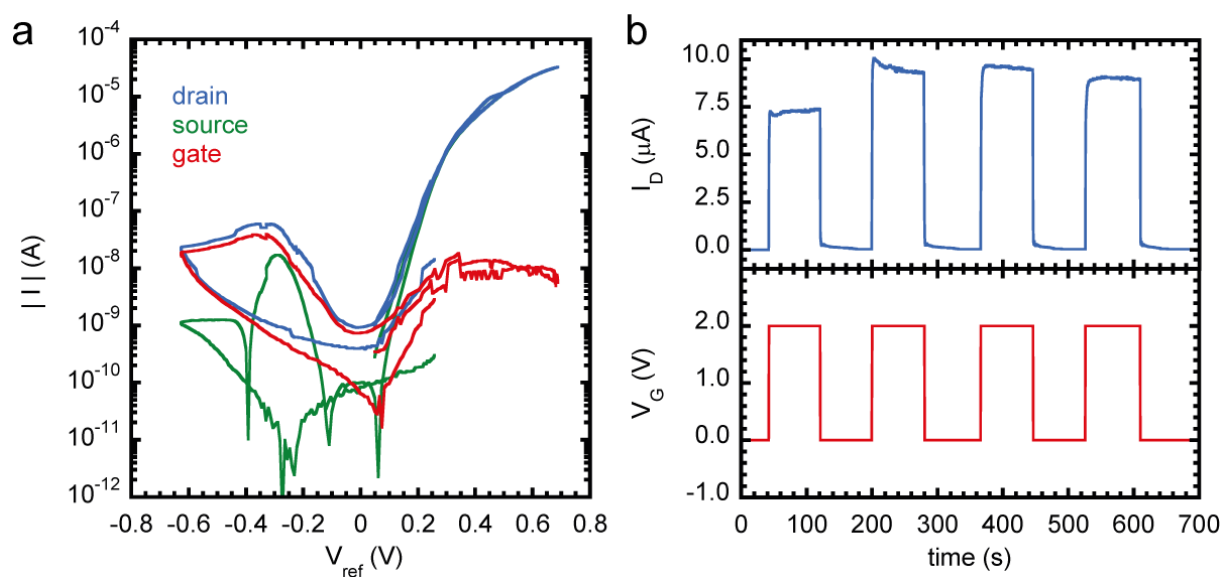


Figure S4. Additional transport properties: a) typical drain, source and gate currents in a PbSe CQD superlattice IGFET; b) Transient behavior of ion-gel-gated PbSe superlattice FETs: the gate has to be loaded and unloaded to reach stable and reproducible threshold and “on” currents.

Sample	Substrate #	Area #	Channel length (μm)	Mobility (cm^2/Vs)
SL-EDA	1	1	3	40.4
		2	5	30.6
		3	5	46.2
		4	5	41.5
	2	1	2	10.1
			5	8.09
			10	7.51
		2	2	10.1
			3	14.8
			5	14.0
			10	16.4
	3	1	2	16.7
			3	13.1
			5	19.8
			10	25.2
		2	3	7.24
		3	2	6.95
SP-EDA	1	1	3	3.92
		2	3	2.63
			5	7.92
		3	5	0.84
SL-EDT	1	1	5	2.47
	2	1	3	2.27
			5	5.11
		2	3	6.26
			5	4.21
SL-TBAI	1	1	5	10.9
		2	5	3.12
SL-OA	1	1	5	7.17
		2	3	4.90
			5	8.42
		3	5	2.26

Table S1. Mobility values calculated from the collected transfer curves, indicating which devices belong to the same substrate and the location.

Contact resistance analysis

Contact resistances were calculated using the transfer line method. Devices of the same set with several different channel lengths were measured, and the total resistances at the same effective gate voltage $\Delta V = V_g - V_{th}$ were plotted against the channel length. The contact resistance (R_c) is obtained by a linear fit:

$$R_{tot} = R_c + \frac{L}{\mu C W \Delta V} \quad (S1)$$

where L and W are the channel length and width, C is the gate capacitance, and μ is the mobility. The contactless mobility (μ_0) can then be calculated as:

$$\mu_0 = \frac{\partial(\frac{\partial R_{tot}}{\partial L})^{-1}}{\partial V_g} \frac{1}{C W} \quad (S2)$$

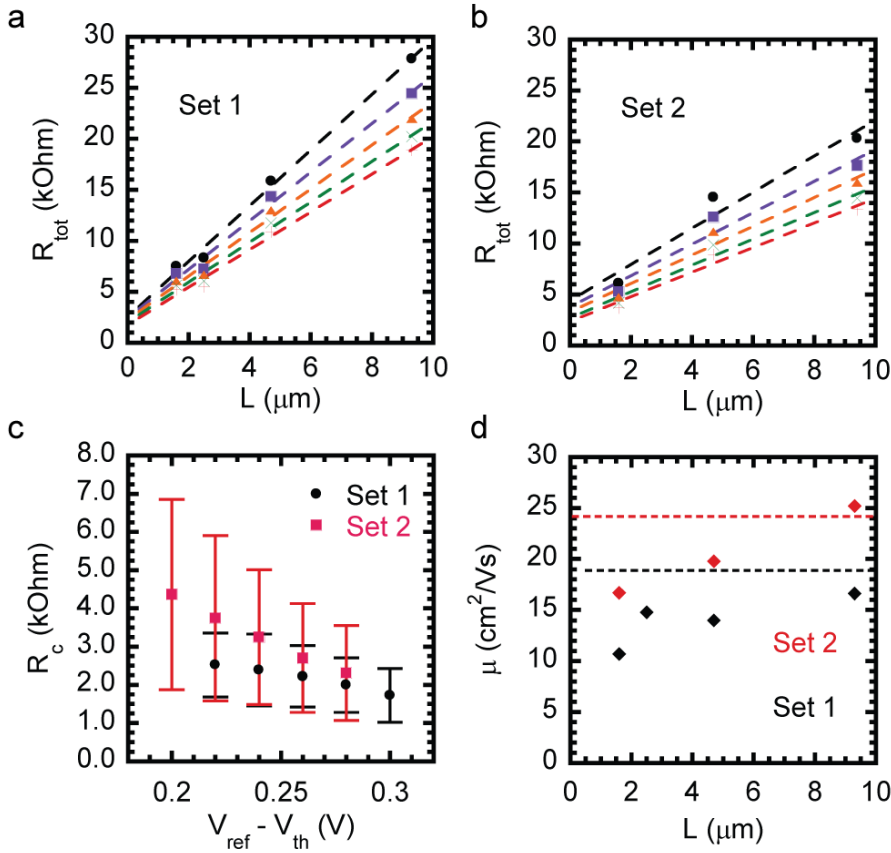


Figure S5. Transfer line method determination of the contact resistance and contactless mobility in two sets of PbSe superlattice FETs: (a,b) resistance vs channel length in devices in proximity; (c) the resistance decreases with increasing carrier concentration, and is similar in both sets of devices; (d) contactless mobility values (dashed line) 10-80% higher than the raw data (markers) are calculated for the two sets following Equation S2.

Ion gel capacitance measurements

The capacitance of the ion gel was measured forming larger area capacitors between flat electrode surfaces. Four bottom electrodes were used: ITO, gold, gold with a monolayer of PbSe and gold with the multilayer PbSe used in the research. The substrate/bottom electrode was covered with a droplet of the ion gel, dried the same way as the devices, and a Pt foil electrode was placed on top. In case of the ITO substrate, droplets of several size were formed and in total 5 electrode pairs were characterized. For the gold-based samples, two top electrodes of different size were placed on top of the same droplet. The impedance data between 10 mHz and 100 Hz were fitted with the theoretical expression for a constant phase element (CPE) for each set of data (see Equation S3). To determine the effective capacitance (C_{eff}), the imaginary part of the CPE impedance as a function of frequency was expressed as the impedance of a capacitor, and the values were calculated at 63 mHz frequency, equivalent to the 5 mV/s rate used in the FET measurements) using Equation S4:

$$Z_{CPE} = Qf^a * e^{-i\pi a} \quad Z_{C,eff} = Im(Z_{CPE}) \quad Z_{C,eff} = (i2\pi f C_{eff})^{-1} \quad (S3)$$

$$C_{eff} = Q(2\pi f)^{a-1} \sin(-\frac{\pi a}{2}) \quad (S4)$$

Examples for the devices are shown on Figure S6(a-b). The obtained capacitance values are plotted against the effective device area $1/A_{eff} = 1/A_{top} + 1/A_{bottom}$ on Figure S5(c). The slopes were determined by fixing the intercept at 0, and are collected on panel d. The bare gold- and thin PbSe-based samples show very similar slopes around $8 \mu\text{F}/\text{cm}^2$. The ITO-based capacitors behave very similar to the one prepared the same way as out actual samples, with a slope of $6 \mu\text{F}/\text{cm}^2$. The slopes are the average electrode capacitance of that system, and the differences can shed light to differences in the electrode surfaces, for example. In case the ionic liquid fills the pores of the CQD superlattice, a large increase in the actual electrode area is expected, resulting in a much (2-5) times) higher calculated C_{el} than the value measured on bare gold. Since we do not see this effect, we can exclude a “bulk” gating using this ionic gel system. For the mobility calculations, $6 \mu\text{F}/\text{cm}^2$ was used.

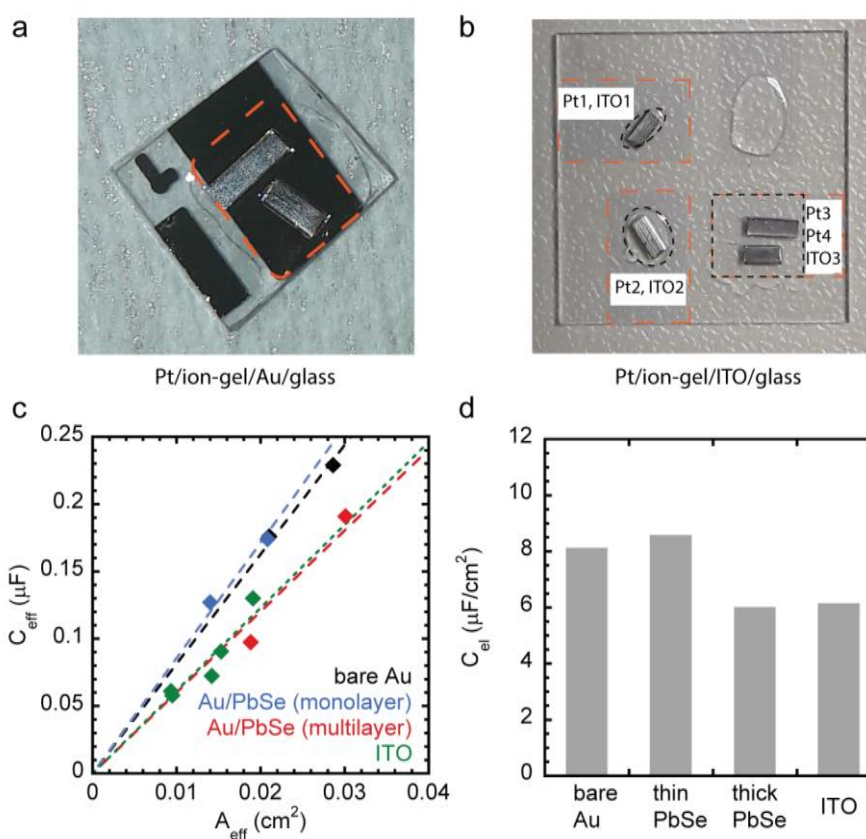


Figure S6. The devices and data used to obtain the capacitance value for the mobility calculation; (a) ion gel sandwiched between bare Au and Pt; (b) ion gel sandwiched between ITO and Pt; (c) effective capacitance values at 63 mHz versus the effective electrode areas, and the linear fits; (d) electrolyte layer capacitance determined using different electrodes.